*instruments*

MDPI

*Article*

# Nearly Monochromatic Bremsstrahlung of High Intensity via Microparticle Targets: A Novel Concept

**Rolf Behling [1,*], Christopher Hulme [2], Panagiotis Tolias [3] and Mats Danielsson [1]**

[1] Particle-, Astrophysics and Medical Imaging Department, KTH Royal Institute of Technology, SE-100 44 Stockholm, Sweden; md@mi.physics.kth.se
[2] Department of Materials Science and Engineering, KTH Royal Institute of Technology, SE-100 44 Stockholm, Sweden; chrihs@kth.se
[3] Department of Space and Plasma Physics, KTH Royal Institute of Technology, SE-100 44 Stockholm, Sweden; tolias@kth.se
* Correspondence: rkobe@kth.se

**Abstract:** As an alternative to rigid anodes, a novel concept of X-ray targets consisting of a stream or a multitude of streams of fast tungsten microparticles has recently been proposed. Low-density microparticle streams resemble thin targets with nearly constant intensity distribution over a wide range of photon energies, abruptly terminating at the Duane–Hunt limit of maximum photon energy instead of falling off smoothly. According to our simulations, fast microparticles outperform classical rigid targets and enable extremely high electronic input power density and X-ray output. This opens new possibilities for generating high-intensity, nearly monochromatic X-rays. Such keV-type X-ray sources could replace expensive electron synchrotrons in appropriate applications. Furthermore, for sufficiently thin microparticle streams, the output X-ray spectra are functions of particle size, allowing modulation of the mean photon energy. We simulated the spectral response of tungsten microparticles using Monte Carlo methods and confirmed the validity of our new concept to generate near-monochrome spectra and high intensity with microparticle-based X-ray sources, outperforming classical X-ray tubes. Furthermore, we confirm a weak size dependence of the mean energies of filtered X-rays. We complement previous results highlighting the advantages of microparticle-based X-ray targets and aim at the implementation of the new concept in the future.

**Keywords:** X-ray source; X-ray tube; spectral imaging; microparticle target; monochromatic X-rays; rotating anode; tungsten; medical imaging; non-destructive X-ray testing



**Citation:** Behling, R.; Hulme, C.; Tolias, P.; Danielsson, M. Nearly Monochromatic Bremsstrahlung of High Intensity via Microparticle Targets: A Novel Concept. *Instruments* **2024**, *8*, 42. https://doi.org/10.3390/instruments8030042

Academic Editor: Antonio Ereditato

Received: 31 July 2024
Revised: 30 August 2024
Accepted: 7 September 2024
Published: 13 September 2024



## 1. Introduction

### 1.1. Quest for Nearly Monochromatic X-Spectra

For many applications, such as source-based spectral X-ray imaging or X-ray fluorescence imaging, a major shortcoming of the spectra of unfiltered bremsstrahlung from thick targets is their wide energetic bandwidth, determined by the target material and the tube voltage. For example, the full width at half maximum (FWHM) of the intensity distribution of photon energies for a 150 kV tube voltage and a thick tungsten target behind a typical 2.5 mm aluminum medical diagnostic filter, as a percentage of the median of 58 keV, is 138%. Instead, spectrally tuneable monochromatic radiation would be highly desirable in medical imaging to minimize the patient's X-ray dose, notably the skin dose, while maximizing the contrast-to-noise ratio depending on the imaging task [1,2]. In conventional film-based mammography, characteristic K-radiation, e.g., from molybdenum, has been used to significantly reduce the bandwidth through molybdenum filters that block radiation beyond the K-edge [2]. However, the low melting point of molybdenum limits the photon output, and the mean photon energy cannot be electronically manipulated without switching the elementary composition of the target material and the filter, such as to rhodium, which enables slightly reduced patient attenuation.

A number of other applications require extremely narrow bandwidths to reduce background noise. One example is X-ray fluorescence imaging (XFI), which is currently investigated assuming radiation from expensive synchrotrons or a Thomson scatter source [3–6]. Figure 1 of [6] compares measured and simulated spectra, based on the assumption of monochromaticity, as delivered by the envisioned synchrotron (Petra III, DESY, Hamburg, Germany). If the spectrum had a bandwidth larger than 15% FWHM, the Compton peak from single Compton scattering and the left flank (see Figure 1 of [6]) of it, originating from multiple Compton scattering, would be excessively broadened and begin overlaying and suppressing the weak X-ray fluorescence signal. Furthermore, if the incident spectrum were even as broad as from a typical X-ray tube, then the resulting XFI spectrum would just be very similar to this incident spectrum, and therefore, the weak XFI fluorescence lines could not be measured against the spectral background in their signal regions, hence rendering high-sensitivity XFI measurements impossible.

To produce a sufficiently narrow spectrum, thick target bremsstrahlung sources with extremely strong filters may be employed. However, this measure comes at the expense of photon flux. A higher photon fluence and small bandwidth would be very desirable for the cited preclinical research and similar to reduce the exposure time to a biologically acceptable level.

### *1.2. Thin X-ray Targets*

Bremsstrahlung sources with a conversion layer thinner than the electron stopping range offer a remarkable advantage [7]. Unlike thick targets, where slowed electrons cause pollution of the spectrum with low-energy photons, the output intensity distribution is nearly flat over the entire energy range with a sharp drop at the Duane–Hunt limit, that is, the maximum photon energy defined by the tube voltage [7]. The tiny low-energy content allows the reduction of the necessary filtration to monochromatize the spectrum. Consequently, the filtered output intensity per incident primary electron is increased. However, thin targets are typically stationary and consist of micrometer-thin conversion layers, such as from tungsten, on heat-spreader material like diamond or beryllium [8]. The electron current must be reduced by one or two orders of magnitude compared with rotating anode sources.

In comparison, rotating anode tubes can typically produce a higher total filtered photon flux, despite the wasted photons due to additional attenuation by thicker filters. Strongly filtered bremsstrahlung is applied in a variety of medical imaging modalities, such as angiography, with copper thickness of up to 0.9 mm for tube voltages of up to 125 kV. However, the input power density of rotating anodes is limited. The focal track erodes over time by thermal cycling, and the focal track velocity is limited to about 100 m $s^{-1}$ to avoid rotor burst. The heating mechanism is primarily restricted to surface heating of a micrometer-thin top layer. Unfortunately, the development of this target technology has stalled over the recent two decades while at the same time the demand for higher input power density has risen to reduce the focal spot size and improve the spatiotemporal image resolution.

Alternatively, liquid metal anodes yield X-rays of comparatively high brilliance with very small focal spots in the order of 10 µm and a power rating of about 1 kW. However, the liquid target material has a relatively low atomic number. The output is limited by hydrodynamic reasons [9] and typically too small for medical imaging.

### *1.3. Benefits of Microparticle X-ray Targets*

Recently, our group introduced the alternative concept of microparticle-based X-ray targets [10,11]. Without changing the fundamental mechanism of bremsstrahlung generation, we propose to replace the rigid anode with a stream of fast-moving microparticles that interact with the electron beam. Tungsten microparticles of 1 µm diameter and up are commercially available. Several physical factors enable a very high input power density:

- Other than rotating anodes, the tungsten microparticle target does not erode. Therefore, the penetration of electrons and volume heating can be employed to the full extent [12–14].

- The target heat capacity increases drastically with the extended permitted temperature range and the rising specific heat capacity with temperature [15].
- The residence time of the target material in the electron beam can be much shorter than with rigid rotor members [16]. No anode rotor, which would be thermally stressed at high temperatures and temperature gradients, can burst.
- Target heating and cooling are spatially disentangled. This freedom simplifies the design of the vacuum tube.

### *1.4. Challenges for the Implementation of Microparticle Targets*

However, several challenges must be mastered for the implementation of the microparticle target technology. Microparticles may be mechanically and/or electrically accelerated by magnetically levitated spinning particle pumps that operate free of thermal stress at high rotor velocities, such as the rotors of UHV turbo-molecular pumps. The microparticles may enter close to the axis and gain momentum by centrifugal force in radial channels that expel them as a thin stream [11]. Additionally, the electrical (post-)acceleration of microparticle streams has been also investigated for spacecraft propulsion [17] and in the context of high voltage in vacuum [18,19]. Downstream of the interaction region, the heated microparticles may be received by rotary cooling means that slow them down and convey them back, for instance, when gravity exceeds centrifugal force either continuously or after a period of X-ray production, into a principal reservoir [10]. In computed tomography applications [1], gradients of centrifugal acceleration may be employed to convey the microparticles. Alternatively, the tube may be stopped in the top (12 h) position of the CT gantry to let the particles flow back into the reservoir during idle times of the imaging system. To avoid pollution of the high-voltage ceramics for insulation [19], the cathode space should be separated from the target space by a thin electron transparent window. Electric windows comprising biased electrode systems may also be used.

### *1.5. No Blocking Hurdles*

Since, according to our simulations, the most critical potential problem, the charging of the microparticles, can be overcome with available tungsten particles and relevant electron energies, we see no blocking technical hurdle in the way to a technical implementation. The absence of charging enables operating the target without any classic direct electrical connection with the power source. Hence, it is not an anode in classic standard terms. Instead, the X-ray-generating material balances charging by electron backscattering if operated with sufficiently high tube voltages. It resembles legacy glass targets used in the early history of X-ray production.

We envision building high-performance radiographic X-ray tubes and high-output almost monochromatic X-ray sources that combine the spectral benefits of thin targets with the superior X-ray output enabled by high heat capacity and highly efficient convection cooling. Such novel compact tubes may have the potential to replace more expensive X-ray sources such as electron synchrotrons or Thomson sources for many important applications [4] and may also support source-based spectral radiographic imaging [20] in combination with microparticle-based modulation of the X-ray fluence.

## 2. Materials and Methods

### *2.1. Thin X-ray Target Simulation*

We consider heating a stream of moving microparticles that is much thinner than the electron penetration depth in a semi-infinite (thick) microparticle cloud of equal mass density. As opposed to volume heating of a thick stream, that is preferably treated considering the depth distribution of energy loss, such as in [11], we discuss in this study individual microparticles as members of a diluted stream that are small compared with the length of intra-particle heat diffusion in the relevant heating time and are assumed to be rotating and, therefore, isotopically heated by impinging electrons of equal kinetic energy. We further consider the microparticles to be isolated and ignore electron impact from inter-particle

backscattering. The discussed assembly of microparticles may form a monolayer if viewed from the electron source, and, therefore, cover $\pi\sqrt{3}/6 \approx 91\%$ of the cross-section area, i.e., about 9% of the electrons from an orthogonal beam pass without any interaction. An additional fraction of backscattered, transmitted, and de-energized electrons leaves the target. Compared with a thick target, where the electrons are only lost by backscattering and either reversing their initial direction or totally coming to rest, the overall X-ray conversion is smaller. The poor efficiency can at least partially be compensated for if the cathode is able to emit an enhanced electron beam [21,22] and most of the unused electron energy is recuperated through electron collectors that feed back into the electrical cathode supply. This technology is well established for Klystrons and other vacuum electronics [23].

Let $r_{\mu P}$ be the microparticle radius, $\rho_W$ the mass density, $c_W(T)$ the temperature-dependent mass heat capacity of tungsten, and $T_{m,W}$ the melting point. If melting of the microparticles is not accepted, its temperature $T$ may rise from its initial temperature $T_0$ upstream of the interaction region to $T_{m,W}$ at the exit after it was impacted in the region of interception with the electron beam during the residence time $\Delta t$. If we ignore the temperature dependence of $\rho_W$ (which is below 5% in the considered temperature range), the permitted input energy for a single microparticle $E_{max,\mu P}$ is

$$E_{max,\mu P} = \frac{4}{3}\pi {r_{\mu P}}^3 \rho_W \int_{T_0}^{T_{m,W}} c_W(T) \mathrm{d}T \quad (1)$$

The integral is numerically evaluated using Figure 5b of ref. [15], showing a monotonically increasing mass specific heat capacity, namely, beyond 2000 K, that doubles between 700 K and 3695 K and makes high target temperatures specifically attractive. We assume that the interaction region coincides with the electron beam cross section in the plane of the microparticle stream. Widening of the focal spot by electron backscattering can be ignored; as for a thin or diluted stream, the probability of excitation of neighbor microparticles is small compared with the probability of primary impact.

Energy delivery into a microparticle and charge modulation under electron impact are both functions of the primary electron energy. We simulated the percentage of absorbed energy per microparticle and impacting primary electron $S_{\mu P}$ and the percentage of charge captured per impacting electron $q_{\mu P}$ with the Monte Carlo software Casino v.3 [24]. Figure 1 shows $S_{\mu P}$ (left scale) and $q_{\mu P}$ (right scale) for sample tungsten microspheres of 2.5 µm radius. Negative charging turns into slightly positive charging beyond 127.5 keV primary electron energy.

The threshold voltages of charging and the energy pickup at those voltages are shown in Table 1. Almost the entire medical diagnostic tube voltage range is covered with commercially available microparticles. We assume dilute microparticle targets which are much thicker than a single monolayer. Otherwise, higher electron energies would have to be applied to avoid charging, such as about 25 keV extra for a thin compact monolayer of microparticles with a radius of 2.5 µm. The stream thickness may be enlarged to minimize the threshold electron energy. Details will depend on the electrical environment.

**Table 1.** Threshold tube voltages to avoid negative charging for single tungsten microspheres or a dilute microparticle target under electron impact (Monte Carlo simulation).

| Tungsten Microsphere Radius (µm) | Minimal Threshold Tube Voltage to Avoid Negative Charging (kV) | Percentage of Absorbed Energy at the Threshold Tube Voltage (Left Column) |
|---|---|---|
| 0.5 | 43.0 | 12.0% |
| 1.0 | 69.0 | 11.8% |
| 2.5 | 127.5 | 11.2% |
| 4.0 | 174.8 | 11.0% |
| 8.0 | 289.0 | 11.1% |

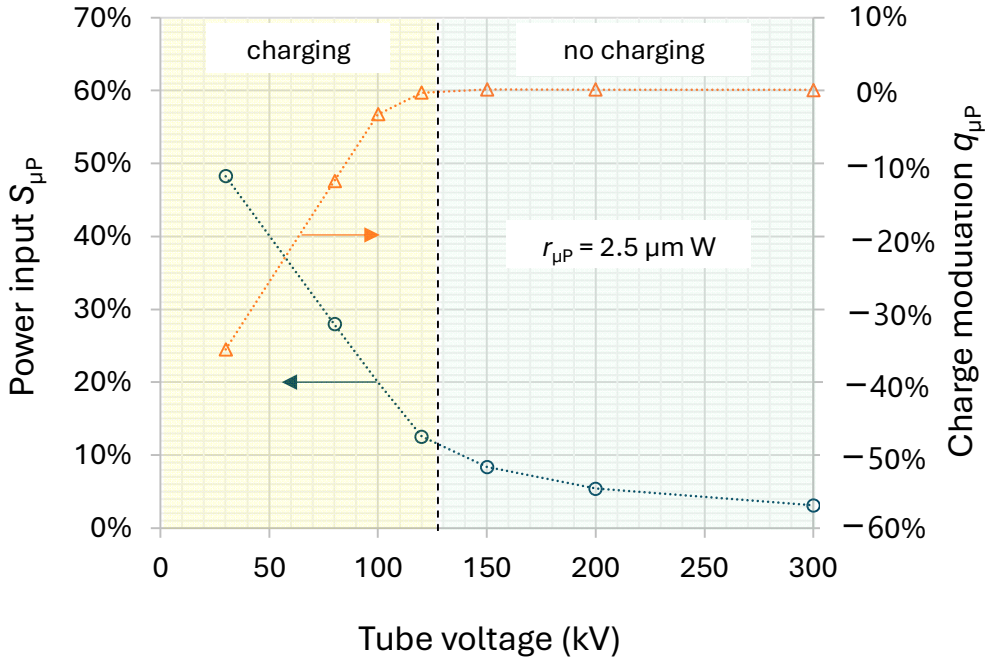


**Figure 1.** Average percentages of charging and energy absorption per impinging electron for single tungsten microspheres with a radius of 2.5 µm, from Monte Carlo simulation. The charge state is stable beyond 127.5 kV tube voltage (right of the dashed center line). Left and right scales apply as indicated by arrows; straight dotted lines are added to guide the eye.

### *2.2. Size-Dependent Spectra*

The maximal X-ray intensity for strongly filtered beams primarily depends on the required filtration, the relationship between filtration and attenuation (mainly determined by the ratio of photoionization vs. Compton scattering), and the thermal performance of the target. In the following, we focus on predicting the potential of microparticle targets to generate highly monochromatic bremsstrahlung. We will discuss the electron source and other technical aspects in future publications.

We consider a very thin stream of microspheres that form a close packed monolayer impacted by an orthogonal electron beam with rectangular cross section. With the length of the electron beam cross section normal to the direction of motion $L_{cs}$, its width $W_{cs}$, the microparticle velocity $v_{\mu P}$, and the residence time $\Delta t = W_{cs}/v_{\mu P}$, the input energy absorbed during transit of a microparticle through the electron beam with current density $j$ equals $\Delta t \cdot U_{tube} \cdot j \cdot \pi {r_{\mu P}}^2 \cdot S_{\mu P}$, with its permitted maximum at $j_{max}$,

$$j_{max} = \frac{I_{FS,max}}{W_{CS} L_{CS}} = \frac{I_{ML,max}}{W_{CS} L_{CS}\, a_{ML}},$$

where $I_{FS}$ denotes the primary electron current in the focal spot. The portion of the electron current $I_{ML}$ that hits microparticles forming the considered monolayer is proportional to the flux of generated X-ray photons. Let the percentage of area covered by the cross sections of microparticles that form the monolayer be $a_{ML}$, with $a_{ML} = \pi\sqrt{3}/6 \approx 91\%$ for dense packing. Thus, $I_{ML} = a_{ML} \cdot I_{FS}$. The maximum energy captured by a microparticle then equals

$$E_{max,\,\mu P} = \Delta t \cdot U_{tube} \cdot \frac{I_{FS,max}}{W_{CS} L_{CS}} \cdot \pi {r_{\mu P}}^2 \cdot S_{\mu P}. \quad (2)$$

We find for the current $I_{ML}$ that is proportional to the X-ray output intensity, with $\Delta t = W_{CS}/v_{\mu P}$,

$$I_{ML,max} = \frac{2\pi\sqrt{3}}{9} \cdot \frac{L_{CS} v_{\mu P}\; r_{\mu P}\, \rho_W}{U_{tube} S_{\mu P}} \cdot \int_{T_0}^{T_{m,W}} c_W(T) \mathrm{d}T. \quad (3)$$

We simulated the photon fluence distribution $c_{x,e}(E_{ph})$ emitted by a single microsphere of radius $r_{\mu P}$ orthogonal to the electron beam in 100 cm distance and given as the number of photons per impinging electron and energy interval for the photon energy $E_{ph}$ with the software code FLUKA v4 [25,26]. The emitted photon fluence $F_x$ per energy interval is then

$$F_x\left(E_{ph}\right) = -c_{x,e}(E_{ph})\ I_{ML,max}/e$$

We calculated the total output intensity by weighting the fluence with $E_{ph}$ and dividing the integral over the entire energy range by the mean energy after filtration using a fit function [27]. We used the software SpekPy [28,29] for comparative simulations of thick targets.

## 3. Results

### *3.1. Particle-Size-Dependent Spectral Imaging*

Large microparticles produce an enhanced percentage of low-energy photons excited by low-energy electrons that remain in the particle instead of being backscattered or transmitted into a vacuum. Hence, thin microparticle streams of varying particle size or density may support multispectral imaging by producing photons of varying mean energies upon changing the microparticle species. To test this hypothesis, we simulated the filtered X-ray output intensity for single microparticles of different sizes at 150 kV tube voltage and compared it with the output from thick tungsten targets of 8° anode angle, Figure 2. We filtered with 2.5 mm aluminum to mimic the primary beam from a typical medical diagnostic X-ray source and with an additional 25 mm aluminum filter that is often used to represent a human being to be imaged, and we assessed the spectrum at the image detector.

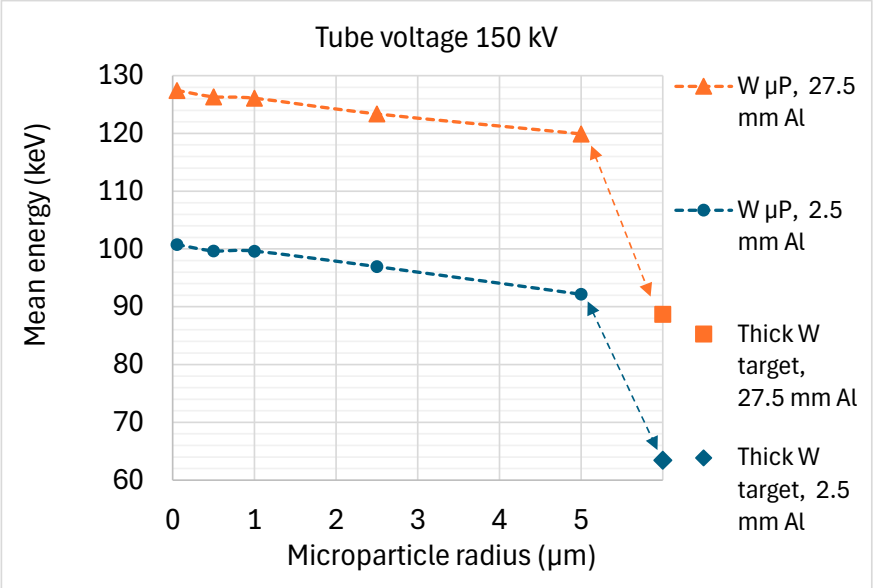


**Figure 2.** The mean output photon energy decreases with microparticle (μP) size for tungsten microparticles and 150 kV tube voltage compared with mean energies from thick tungsten targets. Added aluminum filters are indicated. The 2.5 mm Al applies to the primary beam for medical imaging, and 27.5 mm Al includes 25 mm aluminum filtration to mimic a patient.

Figure 3 shows sample spectra for 1 μm (5 μm) tungsten microspheres. For each impinging electron, the total emitted intensity amounts to $2.8 \times 10^{-7}$ ($1.7 \times 10^{-6}$) keV cm$^{-2}$ in 1 m distance with only the target-intrinsic filter (designated as no filter), respectively, $2.8 \times 10^{-11}$ ($1.6 \times 10^{-10}$) keV cm$^{-2}$ for 27.5 mm added aluminum filter. As shown in Figure 2, the patient equivalent filtration yields a mean energy of 126.3 keV (123.4 keV).

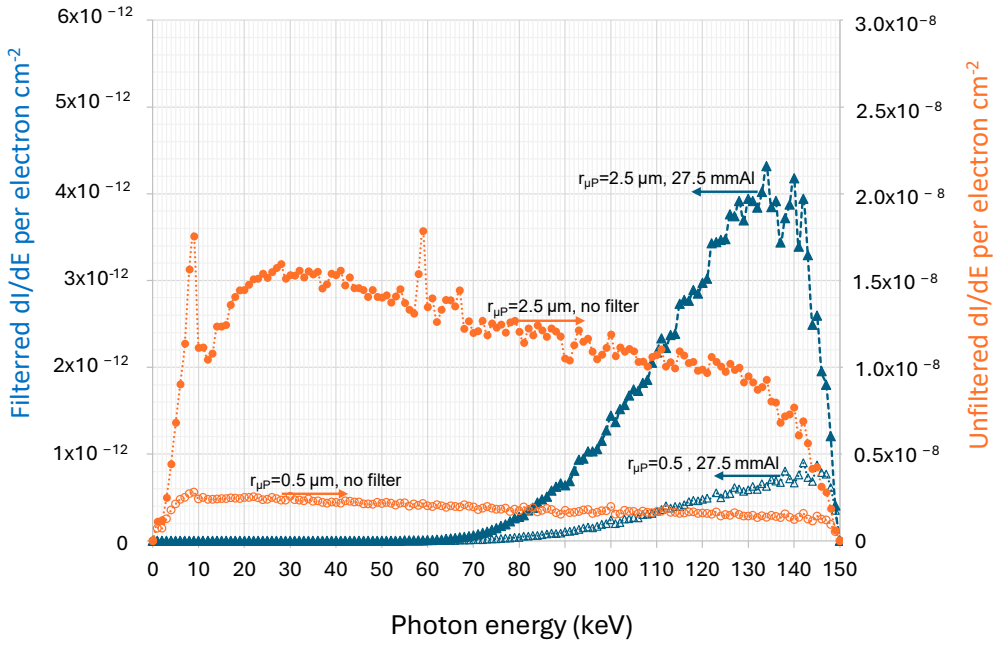


**Figure 3.** Comparison of simulated X-ray intensity (per impinging electron, keV energy interval and $cm^2$ in 1 m distance) for 150 kV tube voltage, generated by tungsten microspheres of 1 µm and 5 µm diameter under electron impact with isotropic current density. The spectra are shown for the particle-intrinsic tungsten filtration only (no filter, right scale) and 27.5 mm added aluminum filter (left scale). Dashed lines are added to guide the eye.

Although the variation in the mean energy is small compared with the bandwidth of the filtered spectra, the phenomenon may help support multispectral imaging with microparticle streams of various particle-size distributions, such as streams supplied through separate accelerator channels. The channel design may enable alternating the mass flow and modulate the conversion efficiency in addition to the modulation by the particle size alone that Figure 3 suggests.

### *3.2. Nearly Monochomatic X-rays with High Intensity*

Figure 4 shows sample spectra of about 277 keV mean energy from further simulations with FLUKA and SpekPy that support our second hypothesis. It shows that microparticle targets are excellent sources of almost monochromatic keV-type X-rays. We filtered the emerging wide-band radiation to yield spectral bandwidths of an intensity of 10% FWHM.

As opposed to thick targets, spectra from dilute microparticle targets contain only a few mid-energy photons. The necessary additional monochromatizing filter and, thus, its attenuation can be kept small, and the output intensity per primary electron is substantially enhanced.

However, the filter materials must be carefully chosen to avoid spectral leaks around K-edges. Preferred are materials, such as tungsten, with strong photoelectric effect and filtering capacity relative to the inherent attenuation. However, tube voltages between 90 and 150 kV may cause additional contributions with photon energies around the K-edges. Therefore, we used aluminum for 30 kV tube voltage, tin for up to 200 kV, and tungsten for 300 kV.

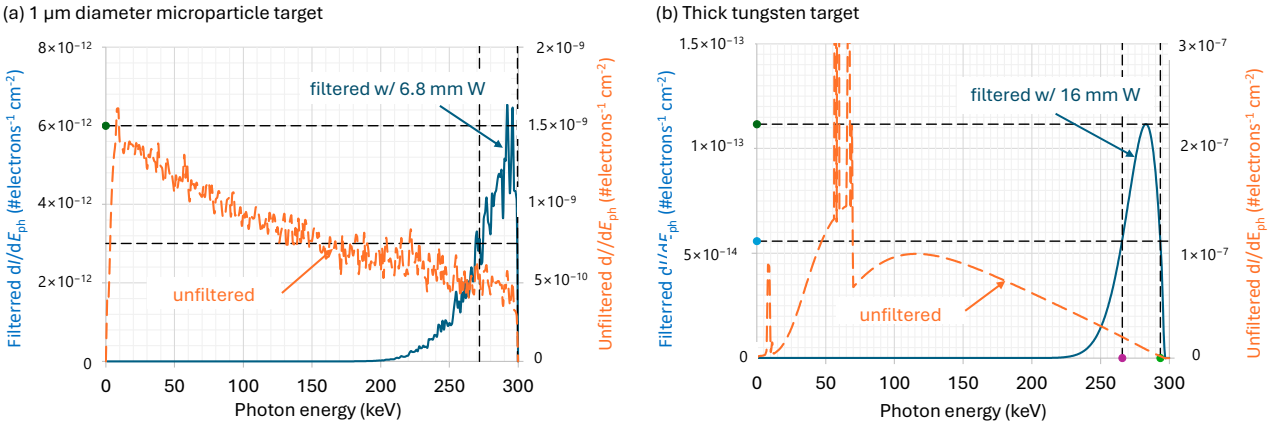


**Figure 4.** Intensity distributions $\mathrm{d}I/\mathrm{d}E_{\mathrm{ph}}$ of bremsstrahlung spectra in # electrons$^{-1}$ cm$^{-2}$ in 1 m distance, unfiltered (intrinsic target filtration only, designated as no filter), and additionally filtered with tungsten to monochromatize to 10% FWHM about the mean value. (**a**) X-rays emitted from a 1 µm diameter tungsten microsphere orthogonal to the impinging electron beam, tube voltage 300 kV, mean energy 277 keV, (right scale), and additionally filtered with 6.8 mm W (left scale); (**b**) X-rays from a thick tungsten target at 8° anode angle, tube voltage 297 kV, mean energy 277 keV (right scale), and filtered with 16 mm tungsten (left scale).

We calculated the permitted tube currents for a source with 1.0 mm long focal spot and 8°, corresponding to a physical length $L_{\mathrm{CS}}$ of 3.593 mm, according to Equation (3), for a microparticle velocity of 400 m s$^{-1}$, and compared it with publicly available data of a rotating frame tube (Siemens-Healthineers Straton®) and a thin target tube [30], Figure 10, left panel, and show the result in Table 2. The public tube data of the reference tube were taken for 20 s CT exposure time and adapted to a physical 1.0 mm long focal spot with isotropic current density according to the surface heating model of Müller and Oosterkamp by assuming that the nominal value according to the standard IEC 60336 [31] would correspond to the same numerical value in millimeters (edge ramps ignored).

**Table 2.** Maximal permitted currents impinging on the monolayer-equivalent target with possibly greater thickness, $I_{\mathrm{ML}}$(A), for 1 mm focal spot size and 400 m s$^{-1}$ microparticle velocity vs. tube voltages $U_{\mathrm{tube}}$ for streams of microparticles with radii from 0.5 to 5 µm and for classical reference tubes: a high-performance thick target rotating frame tube and a thin target tube, adapted from [30].

| $U_{\mathrm{tube}}$ (kV) | Target Current $I_{\mathrm{ML}}$ (Ampere) | | | | | |
|---|---|---|---|---|---|---|
| | 0.5 µm | 1 µm | 2.5 µm | 5 µm | Rotating Frame | Thin Target |
| 30 | 1.4 | 1.8 | 3.3 | 6.8 | 1.27 | 0.20 |
| 80 | 3.1 | 3.0 | 1.7 | 3.3 | 0.48 | 0.08 |
| 120 | 3.9 | 3.8 | 2.1 | 3.0 | 0.32 | 0.05 |
| 150 | 4.3 | 4.3 | 2.7 | 3.5 | 0.25 | 0.04 |
| 200 | 4.9 | 4.8 | 3.6 | 4.2 | 0.19 | 0.03 |
| 300 | 5.5 | 5.5 | 4.9 | 5.4 | 0.13 | 0.02 |

A minimum of the current can be observed in Table 2 for 80 kV at about 2.5 µm radius. The absorbed power in a microparticle increases with size and the allowable current decreases until the diameter exceeds the mean electron scattering range and the electron transmission breaks down. Beyond this transition radius for the indicated tube voltage range at $r_{\mu\mathrm{P}} \approx 2.5$ µm, $S_{\mu\mathrm{P}}$ stabilizes at about the value for thick targets (50–60%). According to Equation (3), the allowable current then increases again with increasing particle radius and heat capacity.

The superior power density of microparticle targets translates to a superior target current in addition to the higher filtered output per impinging electron. Figure 5 shows the

excellent output in terms of fluence in 30 cm distance from the 1 mm × 1 mm focal spot. For comparison, we assume an anode angle of 8° between the plane of X-ray production and the central beam to the center of the detector and equal X-ray output for microparticle targets for an orthogonal (with respect to the electron beam, as simulated) and 8° backwardly angulated central beam.

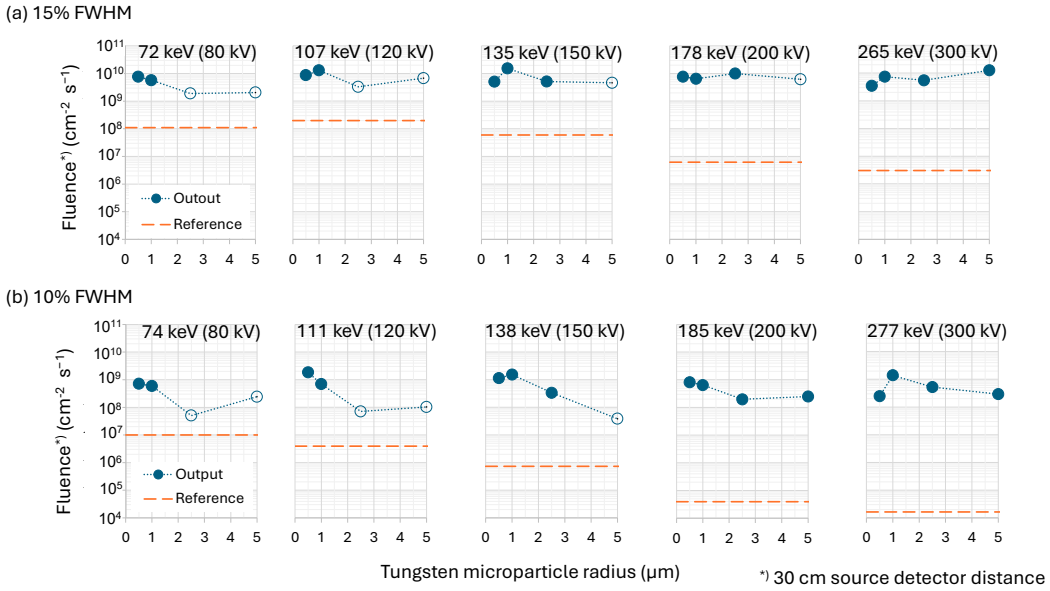


**Figure 5.** Fluence of strongly prefiltered X-rays from dilute tungsten microparticle sources with particle radii from 0.5 to 5 µm for a selection of mean photon energies, 30 cm source–detector distance, and comparison with a thick target high-performance rotating frame reference tube for the tube voltages 80 kV, 120 kV, and 150 kV (in brackets) and a thin target reference tube for 200 kV and 300 kV (no rotating anode reference tube available for comparison, dashed lines). The hollow dots correspond to tube voltages (in brackets) that may cause negative charging. Extra measures would be required to neutralize the particles. (**a**) Filtered for 15% FWHM, (**b**) filtered for 10% FWHM bandwidth (dotted lines added to guide the eye).

The focal spot considered for Figure 5 (1 × 1 mm, 8° anode angle) is typical for diagnostic computed tomography. If only a narrow field of view in the width direction of the target were required (pencil beam), the output fluence could be substantially enhanced by reducing the anode angle and lengthening the focal spot, as the permitted input power is proportional to the focal spot length and independent of the width.

## 4. Discussion

As shown in the Introduction, and with reference to [4–6], only sufficiently narrow-bandwidth X-ray sources enable XFI measurements with the sensitivity required by biomedical applications, especially for in vivo measurements. Among other purposes in medical imaging, the presented concept serves to replace expensive synchrotrons or laser-wakefield sources for dedicated applications like XFI.

We are convinced that with the establishment of the new paradigm of X-ray targets, viable technical solutions will be found, as the fundamental hurdles have been explored with encouraging results.

The implementation of the microparticle X-ray source technology will require substantial development effort. Due to electrical repulsion, pure electrostatic microparticle accelerators would not allow the stream to be sufficiently focused into a small interaction region. Therefore, mechanical microparticle accelerators or pre-accelerators are required. Fortunately, unlike rotating anodes, magnetic bearings without any electric current contacts could be used, since the microparticles lift off uncharged. An electron window opaque to microparticles would be required to shield the cathode region for reasons of high-voltage

stability. We have shown that the microparticle stream can operate in a fundamentally neutral manner. The charge of the microparticles entering the interaction region is approximately equal to the charge at the exit. We showed in a previous publication [11] that discharge mechanisms such as electron field emission or thermionic emission of hot particles could be available to resolve deviations in the electrical potential of the microparticles. Another way to adjust the tube voltage would be to control the cathode voltage. Due to the absence of moisture, even micron-sized microparticles are expected to be sufficiently mobile in ultrahigh vacuum. In addition to previous work [11], we will develop further transport and recycling mechanisms. For example, we plan to collect hot microparticles using rotating elements that enclose the target space, fill a reservoir, and return the particles to the central area of the rotary accelerator during a break in X-ray production.

## 5. Conclusions

We demonstrated through previous Monte Carlo and finite element method simulations the benefits of replacing the classical rotating X-ray anode with a stream of microparticles. Not only the possible power density but also the spatiotemporal image resolution could be much higher. We also see technical solutions. We showed in this study the benefits for spectral X-ray imaging and the generation of high-intensity, narrow-bandwidth X-rays that could replace electron synchrotrons or other expensive sources for many applications.

## 6. Patents

Particle-based X-ray source: US11882642B2; US2023209693A1, WO2023128856A1.

**Author Contributions:** Conceptualization, methodology, investigation, writing—original draft preparation, R.B.; writing—review and editing, C.H. and P.T.; X-ray spectrum simulation: Gavin Poludniowski, Karolinska Institutet, 171 77 Stockholm, Sweden; supervision, M.D. All authors have read and agreed to the published version of the manuscript.

**Funding:** This research received no external funding.

**Data Availability Statement:** Data are available on request from the author.

**Conflicts of Interest:** Mats Danielsson is the owner of Innovicum, Sweden. The company is the assignee of a relevant patent application. Rolf Behling is the owner of XtrainingX, Technical Consulting (www.XtrainingX.com, accessed on 10 September 2024). and named as inventor for a relevant patent application. All other authors declare no competing interests.

## References

1. Hsieh, J. *Computed Tomography: Principles, Design, Artifacts, and Recent Advances*; SPIE: Bellingham, WA, USA, 2015.
2. Russo, P.E. *Handbook of X-ray Imaging—Physics and Technology*, 1st ed.; CRC Press: Boca Raton, FL, USA, 2018.
3. Kumar, K.; Fachet, M.; Hoeschen, C. High-Spatial-Resolution Benchtop X-ray Fluorescence Imaging through Bragg-Diffraction-Based Focusing with Bent Mosaic Graphite Crystals: A Simulation Study. *Int. J. Mol. Sci.* **2024**, *25*, 4733. [CrossRef] [PubMed]
4. Grüner, F.; Blumendorf, F.; Schmutzler, O.; Staufer, T.; Bradbury, M.; Wiesner, U.; Rosentreter, T.; Loers, G.; Lutz, D.; Richter, B.; et al. Localising functionalised gold-nanoparticles in murine spinal cords by X-ray fluorescence imaging and background-reduction through spatial filtering for human-sized objects. *Sci. Rep.* **2018**, *8*, 16561. [CrossRef] [PubMed]
5. Brümmer, T.; Debus, A.; Pausch, R.; Osterhoff, J.; Grüner, F. Design study for a compact laser-driven source for medical X-ray fluorescence imaging. *Phys. Rev. Accel. Beams* **2020**, *23*, 031601. [CrossRef]
6. Staufer, T.; Körnig, C.; Liu, B.; Liu, Y.; Lanzloth, C.; Schmutzler, O.; Bedke, T.; Machicote, A.; Parak, W.J.; Feliu, N.; et al. Enabling X-ray fluorescence imaging for in vivo immune cell tracking. *Sci. Rep.* **2023**, *13*, 11505. [CrossRef] [PubMed]
7. Dyson, N.A. *X-rays in Atomic and Nuclear Physics*, 2nd ed.; Cambridge University Press: Cambridge, UK, 1990. [CrossRef]
8. Ihsan, A.; Heo, S.H.; Cho, S.O. Optimization of X-ray target parameters for a high-brightness microfocus X-ray tube. *Nucl. Instrum. Methods Phys. Res. B* **2007**, *264*, 371–377. [CrossRef]
9. Hemberg, O.; Otendal, M.; Hertz, H.M. Liquid-metal-jet anode electron-impact x-ray source. *Appl. Phys. Lett.* **2003**, *83*, 1483–1485. [CrossRef]
10. Rolf, B.; Mats, D. Particle Based X-ray Source. US11882642B2, US11882642B2 (A1), 23 January 2024.
11. Behling, R.; Hulme, C.; Tolias, P.; Poludniowski, G.; Danielsson, M. Microparticle Hybrid Target Simulation for keV X-ray Sources. *Instruments* **2024**, *8*, 32. [CrossRef]

12. Whitaker, S. The effect of volume heating. In *Proceedings of the SPIE 0914, Medical Imaging II*; Dwyer, I.S.J., Schneider, Samuel, J., Eds.; SPIE: Bellingham, WA, USA, 1988; pp. 565–576. [CrossRef]
13. Whitaker, S. *Thermal Analysis of Solid, Rotating, X-ray Tube Anodes: New Results and a Comparison with Prior Studies*; Dwyer, S.J., III, Schneider, R.H., Eds.; SPIE: Bellingham, WA, USA, 1984; pp. 285–293. [CrossRef]
14. Winter, J.; Dimroth, A.; Roetzer, S.; Zhang, Y.; Krämer, K.; Petrich, C.; Matejcek, C.; Aulenbacher, K.; Zimmermann, M.; Combs, S.E.; et al. Heat management of a compact x-ray source for microbeam radiotherapy and FLASH treatments. *Med. Phys.* **2022**, *49*, 3375–3388. [CrossRef] [PubMed]
15. Tolias, P. Analytical expressions for thermophysical properties of solid and liquid tungsten relevant for fusion applications. *Nucl. Mater. Energy* **2017**, *13*, 42–57. [CrossRef]
16. Behling, R. *Modern Diagnostic X-Ray Sources*, 2nd ed.; CRC Press: Boca Raton, FL, USA, 2021. [CrossRef]
17. Trottenberg, T.; Kersten, H.; Neumann, H. Feasibility of electrostatic microparticle propulsion. *New J. Phys.* **2008**, *10*, 063012. [CrossRef]
18. Ejiri, H.; Kumada, A.; Hidaka, K.; Donen, T.; Kokura, K. Monte Carlo simulation of microparticle motion in vacuum gap. *Electr. Eng. Jpn.* **2018**, *206*, 32–41. [CrossRef]
19. Latham, R. (Ed.) *High Voltage Vacuum Insulation*; Academic Press: New York, NY, USA, 1995.
20. Hsieh, J.; Flohr, T. Computed tomography recent history and future perspectives. *J. Med. Imaging* **2021**, *8*, 052109. [CrossRef] [PubMed]
21. Gaertner, G. *Modern Developments in Vacuum Electron Sources*; Springer International Publishing AG: Cham, Switzerland, 2020.
22. Gaertner, G.; Barratt, D. New developments and life aspects of oxide and barium dispenser cathodes. In *ITG Fachbericht. Proceedings of the Information Technology Society of VDE 183, May 3–4*; VDE-Verlag: Bad Honnef, Germany; Berlin, Germany, 2004.
23. Raj, A.; Kant, D.; Bandyopadhyay, A.K.; Joshi, L.M. Optimization of grooved klystron collector design for efficient heat transfer. *Int. J. RF Microw. Comput.-Aided Eng.* **2019**, *29*, e21950. [CrossRef]
24. Demers, H.; Poirier-Demers, N.; Couture, A.R.; Joly, D.; Guilmain, M.; de Jonge, N.; Drouin, D. Three-dimensional electron microscopy simulation with the CASINO Monte Carlo software. *Scanning* **2011**, *33*, 135–146. [CrossRef] [PubMed]
25. Battistoni, G.; Boehlen, T.; Cerutti, F.; Chin, P.W.; Esposito, L.S.; Fassò, A.; Ferrari, A.; Lechner, A.; Empl, A.; Mairani, A.; et al. Overview of the FLUKA code. *Ann. Nucl. Energy* **2015**, *82*, 10–18. [CrossRef]
26. Ahdida, C.; Bozzato, D.; Calzolari, D.; Cerutti, F.; Charitonidis, N.; Cimmino, A.; Coronetti, A.; D'alessandro, G.L.; Servelle, A.D.; Esposito, L.S.; et al. New Capabilities of the FLUKA Multi-Purpose Code. *Front. Phys.* **2022**, *9*, 788253. [CrossRef]
27. Orlic, I.; Loh, K.K.; Sow, C.H.; Tang, S.M.; Thong, P. Parametrization of the total photon mass attenuation coefficients in the energy range 0.1–1000 keV. *Nucl. Instrum. Methods Phys. Res. B* **1993**, *74*, 352–361. [CrossRef]
28. Poludniowski, G.; Landry, G.; DeBlois, F.; Evans, P.M.; Verhaegen, F. *SpekCalc*: A program to calculate photon spectra from tungsten anode x-ray tubes. *Phys. Med. Biol.* **2009**, *54*, N433–N438. [CrossRef] [PubMed]
29. Poludniowski, G.; Omar, A.; Bujila, R.; Andreo, P. SpekPy v2.0—A software toolkit for modeling x-ray tube spectra. *Med. Phys.* **2021**, *48*, 3630–3637. [CrossRef] [PubMed]
30. Tan, Y.; Chen, Q.; Zhou, S.; Henriksen, E.A.; Zhang, T. Design and optimization of thin-film tungsten (W)-diamond target for multi-pixel X-ray sources. *Med. Phys.* **2022**, *49*, 5363–5373. [CrossRef] [PubMed]
31. International Electrotechnical Commission (IEC). *IEC 60336, 5th ed.—Electrical and Loading Characteristics of X-ray Tube Assemblies for Medical Diagnosis*, 5th ed.; International Electrotechnical Commission: Geneva, Switzerland, 2020.